the impactor could be "magnetically hanged", through a fixed, thin horizontal plastic plate, from the lower end of a vertical iron rod that initially touched the upper face of the fixed plate. When the rod was lifted up using a computer-controlled electro-mechanical device, the impactor was dropped onto the granular system with very small lateral tilting. The impactor was always released from a height where its lower end was just "touching" the free granular surface.

In the experiment, the vertical acceleration of the impactor was recorded in real time during its penetration into the granular medium (its horizontal acceleration was negligible compared to that along *z*).

RESULTS AND DISCUSSION

Fig. 1 shows the evolution of the vertical acceleration, velocity and position of the sphere as it penetrates the granular matter for HGM (left column) and SGM (right column). Velocity and position graphs were obtained after one and two integrations, respectively, of the acceleration vs. time graph -i.e., the direct output from the accelerometer. The insets have been constructed by plotting the acceleration vs. the calculated position. The positive direction is taken downwards.

Let us examine Figs 1 (a) and (d), as time increases. Initially, $a = 0$, which indicates that the impactor is hanging from the release system. The release process takes less than 70 *ms* both for HGM and SGM, and occurs before the impactor has dropped to a depth of 0.5 *cm* (as suggested by the insets). Then, the downward acceleration increases to average maximum values of $8 \pm 1\ m/s^2$ for HGM and $9 \pm 1\ m/s^2$ for SGM (ideally it should reach $9{,}8\ m/s^2$, but the ball is touching the granular surface before being released). After that, *a* increases in the upwards direction due to the action of granular resistance, reaching average minima of $8 \pm 1\ m/s^2$ for HGM and $9 \pm 1\ m/s^2$ SGM respectively. Finally, zero acceleration is reached, meaning that the sphere has stopped moving (in the case of SGM, $a = 0$ only after a few damped oscillations). The final stage of the stopping process occurs sharply within a few-*mm* distance. A major difference between the two media is the duration of the whole process from release to stop: 340 ± 10 *ms* for HDM, and 470 ± 20 *ms* for SGM.

Figs 1 (b) and (e) show the velocity records resulting from integrating in time the acceleration. In both cases, velocity starts at zero, and reaches maxima of $0.7 \pm 0.1\ m/s$ and $1.0 \pm 0.1\ m/s$ for HGM and SGM, respectively. Then, it goes back to zero quite symmetrically in time.

Figs 1 (c) and (f) show the *z*-position resulting from the integration of the velocity records. In the case of HGM, the depth inside the granular matter goes from zero (at the surface) to $0.14 \pm 0.01\ m$ (approximately in the middle of the granular column). In the case of the SGM, the final depth gives $0{,}22 \pm 0{,}01\ m$ (we checked both values using a thin thread attached to the sphere). Notice that, in the latter case, the ball stops only 4 *cm* from the bottom of the bucket. The damped oscillations of the acceleration at the end of the penetration process may be related to a jammed (more compacted) section of the granular material produced by the impactor itself immediately under it, which acts as a "solid wall". The process is probably enhanced by the proximity of the bottom wall in the case of SGM.

All in all, we have shown that, when a granular system is compacted in such a way that the filling factor decreases just to 94% of its original value, the total penetration time can be reduced to a 70%, the maximum velocity of the impactor can decreased to a 70%, and its maximum penetration depth can be reduced to a 60% of its initial value.

It has been shown before that the equation of motion for penetration of a spherical intruder into a larger system analogous to our SGM can be written as [7]

$$m\frac{d^2z}{dt^2} = mg - \eta\left(\frac{dz}{dt}\right)^2 - \kappa\lambda\left(1 - e^{-\frac{z}{\lambda}}\right), \tag{1}$$

where *m* and *z* are the mass of the sphere and the penetration depth from the free surface, respectively, λ is a characteristic length of the order of the diameter of the container, and the coefficients η and κ characterize the inertial drag, and a depth-dependent friction, respectively. This equation follows well most of the motion [7], but it cannot describe the release process at the very beginning and the final stopping stage (where the acceleration goes suddenly to zero when the ball stops in the bulk of the granular system).

In order to estimate parameters, we use two expressions associated to the motion far from its ends. From (1), it is not difficult to see that

$$\kappa = m\left|s_{a\to 0}\right| e^{z_{a\to 0}/\lambda}, \tag{2}$$

where $s_{a\to 0}$ and $z_{a\to 0}$ are the slope of the *a* vs. *z* graph (see insets), and the depth of the impactor when the acceleration approaches zero, respectively. Assuming $\lambda \sim 0.3\ m$ the resulting values for HGM and SGM cannot be clearly differentiated, and give a value of $\kappa = 1.9 \pm 0.3\ kg/s^2$, which is near the value reported in [7] for a 6-*m* long cylinder with SGM. Additionally,

$$\eta = \frac{1}{v_{\max}^2}\left[mg - \kappa\lambda\left(1 - e^{-z_{v_{\max}}/\lambda}\right)\right], \tag{3}$$

where $v_{\max}$ is the maximum speed of the impactor during penetration, and $z_{\max}$ is the depth at which the ball experiences that speed. Equation (3) gives $\eta_{\mathrm{HGM}} = 0.16 \pm 0.02\ kg/m$ for HGM and $\eta_{\mathrm{SGM}} = 0.05 \pm 0.02\ kg/m$ for SGM. The latter value is close to that estimated in [7].

CONCLUSION

We have shown that, when a granular system is compacted, a small increase in compaction produces an increase in the penetration time, a decrease in the total penetration depth, and a sizable increase in the inertial drag coefficient.

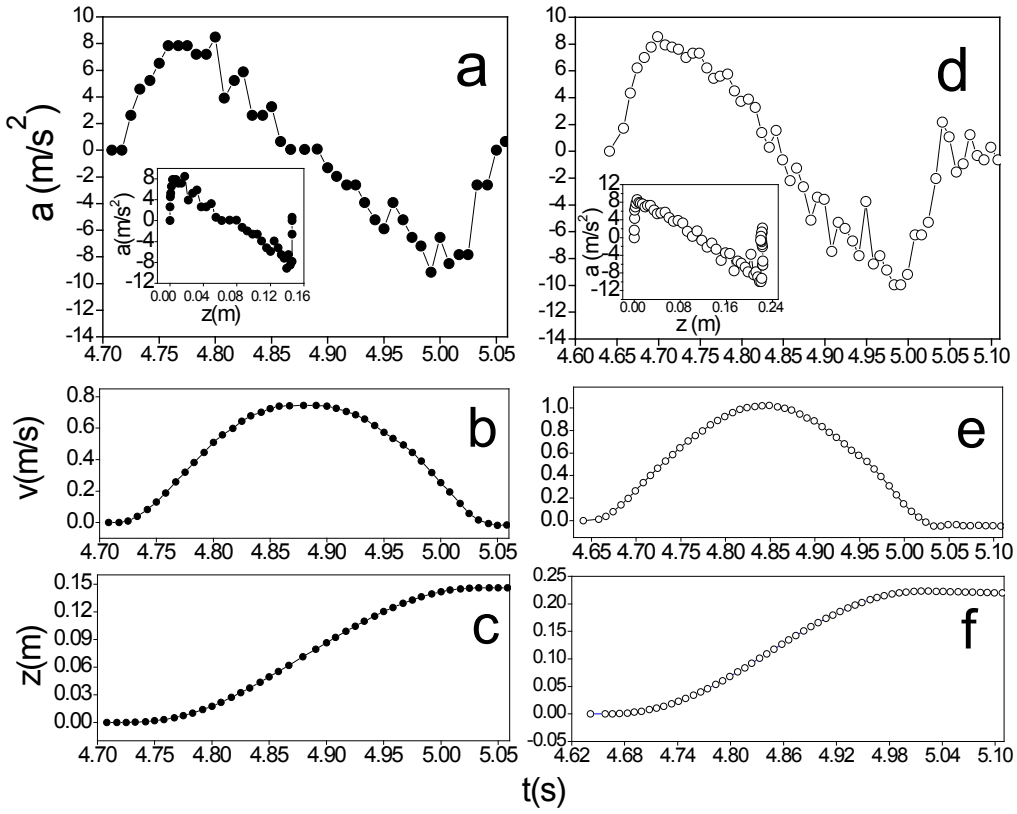

Figure 1: Experimental results. (a) - (c) Vertical acceleration, velocity and position of the impactor vs. time graphs, respectively, for Hard Granular Matter (inset is Acceleration vs. position). (d) - (f) Analogous graphs for Soft Granular Matter. Positive reference points downward.

ACKNOWLEDGEMENTS

We acknowledge C. Pérez-Penichet for contributing to the electronics, O. Ramos, J. Wu and C. Ruiz-Suárez for support in the experimental setup, and A. Batista-Leyva, L. P. Kadanoff and S. Waitukaitis for useful discussions.

[1] J. S. Uehara, M. A. Ambroso, R. P. Ohja and D. J. Durian, Phys. Rev. Lett. **90**, 194301 (2003).
[2] A. M. Walsh, K. E. Holloway, P. Habdas and J. R. de Bruyn, Phys. Rev. Lett. **91**, 104301 (2003).
[3] S. J. de Vet and J. R. de Bruyn, Phys. Rev. E. **76**, 041306 (2007).
[4] J. F. Boudet, Y. Amarouchene, and H. Kellay, Phys. Rev. Lett. **96**, 158001 (2006).
[5] H. Katsuragi and D. Durian, Nat. Phys. **3**, 420 (2007).
[6] D. I. Goldman and P. Umbanhowar, Phys Rev. E **77**, 021308 (2008).
[7] F. Pacheco-Vázquez, G. A. Caballero-Robledo, J. M. Solano-Altamirano, E. Altshuler, A. J. Batista-Leyva and J. C. Ruiz-Suárez, Phys. Rev. Lett. **106**, 218001 (2011).
[8] See MMA7660FC ZSTAR3 accelerometer details at www.freescale.com/zstar
[9] T. Brzinski and D. J. Durian, Soft Matter **6**, 3038 (2011).
[10] D. J. Constantino, J. Bartell, K. Scheidler and P. Schiffer, Phys. Rev. E **83**, 0011305 (2011)**.**

TSALLIS FORMALISM IN RADIOBIOLOGY

EL FORMALISMO DE TSALLIS EN LA RADIOBIOLOGÍA

O. Sotolongo-Costa[a †] and O. Sotolongo-Grau[b ‡]

a) "Henri Poincarè" Group of Complex Systems, Physics Faculty, University of Havana, 10400 Havana, Cuba, osotolongo@fisica.uh.cu†
b) Departamento de Física-Matemática y Fluidos, UNED, Madrid, osotolongo@dfmf.uned.es‡
†, ‡ corresponding authors

We describe how Tsallis' formalism can be applied to the cell survival factor of cells under radiation. Some universal characteristics become revealed with this treatment. This viewpoint has potential applications in clinical radiotherapy.

Describimos cómo el formalismo de Tsallis puede ser aplicado al estudio del factor de supervivencia de células sometidas a radiación. Este tratamiento revela algunas características universales del proceso, y posee aplicaciones potenciales en radioterapia clínica.

PACS: Cell processes, 87.17.-d; dosimetry/exposure assessment of ionizing radiations, 87.53.Bn; radiations effects on biological systems, 87.50.-a

INTRODUCTION

Radiobiologists have developed some empirical models describing the interaction between radiation and living tissues (see [1] for a review of radiobiology models) capable of finding the survival fraction, F_s, of cells under a radiation dose, D.

Their applicability limits are not clear, so multiple corrections have been developed in order to fit the experimental data. Usually expressed as $E = -\ln(F_s)$, the tissue effect gathers together several models of interaction between cells and ionizing radiation. In the linear model, tissue effect is considered linear to the radiation dose, $E = \alpha D$, and the survival fraction, $F_s = \exp(-\alpha D)$, is the cumulative survival probability of a cell under any dose D. So, the probability fulfills the additive property, so $F_s[D_1 + D_2] = F_s[D_1] + F_s[D_2]$. However, this model only fits the experimental data for some tissues under low radiation doses [1], so the tissue effect must be corrected to $E = \alpha D + \beta D^2$, called the linear quadratic (LQ) model. But then the survival fraction loses the additive property. Then, the superposition principle is not fulfilled. However, any model of interaction between radiation and living tissues must allow dividing a continuous radiation in finite intervals and the resultant tissue effect must be the same. Indeed, assuming that the dose is additive, the tissue effect is not the sum of the effects for different doses. This suggests that the radiobiological problem must be approached from a non extensive formulation [2]. Here, a general expression for survival fraction is found using the Tsallis entropy [3] definition, and assuming the existence of a critical dose that kills every single cell. This survival fraction expression fits the experimental data even where previous empirical models fail. Using the q-algebra [4, 5] a new expression to find the survival fraction of a whole treatment is shown.

TSALLIS APPROACH TO RADIOBIOLOGY

To apply the maximum entropy principle in the Tsallis version to the problem of finding the survival fraction of a living tissue [6] that receives a radiation, we postulate the existence of some amount of absorbed radiation D_0 (or its equivalent "minimal annihilation effect", $E_0 = \alpha_0 D_0$) after which no cell survives. The application of the maximum entropy principle performs like the usual one but with a few modifications.

The Tsallis entropy is

$$S_q = \frac{1}{q-1}\left(1 - \int_0^{E_0} p^q(E)\, dE\right). \tag{1}$$

The normalization condition is $\int_0^{E_0} p(E)\, dE = 1$, and the q-mean value becomes $\int_0^{E_0} E\, p^q(E)\, dE = \langle E \rangle_q < \infty$.

With this definition, all properties of the tissue and its interaction with radiation become included in $\langle E \rangle_q$ and therefore in E_0.

To calculate the maximum of (1) under the above conditions the well known method of Lagrange multipliers [5] is applied, resulting in

$$F_s(D) = \begin{cases} \left(1 - \frac{D}{D_0}\right)^{\gamma} & D < D_0 \\ 0 & D > D_0 \end{cases} \tag{2}$$

where we introduced $E = \alpha_0 D$, $\gamma = \frac{2-q}{1-q}$, $D_0 = \frac{E_0}{\alpha_0}$. Finally, the LQ model is easily recovered from (2) in the limit $q \to 1$ up to order two in a Taylor series expansion [7, 8].

All the information about the kind of radiation, radiation rate, etc is contained in the phenomenological term D_0, whereas tissues are characterized by γ. The exponent γ in this case, as in phase transitions, determines the universality class.

Tsallis based survival fraction properties. The linear model for the tissue effect [1] implies that if the dose is additive the corresponding survival fraction is multiplicative. It is worth to find a link between the additive property of the dose and the probabilistic properties of the cell survival fraction. Let us use the function: $\exp_\gamma(x) = \left(1 + \frac{x}{\gamma}\right)^\gamma$ and its inverse function: $\ln_\gamma(\exp_\gamma(x)) = x.$ Then, let us introduce the γ-product of two numbers x and y as

$$x \otimes y = \exp_\gamma\left[\ln_\gamma(x) + \ln_\gamma(y)\right] = \left[x^{\frac{1}{\gamma}} + y^{\frac{1}{\gamma}} - 1\right]^\gamma. \qquad (3)$$

Note that these definitions are not essentially different from the q-exponential and q-logarithm presented in [4]. We are just introducing these definitions to simplify the calculations. Let us now define the "generalized tissue effect" $E = -\frac{E_0}{\gamma}\ln_\gamma(F_s).$ We demand this effect to satisfy the additive property. Then the survival fraction, expressed as

$$F_s = \exp_\gamma\left(-\gamma\frac{D}{D_0}\right), \qquad (4)$$

becomes γ-multiplicative. This implies that the statistical independence of the survival fractions is only possible when $\gamma \to \infty$ ($q \to 1$).

The survival fraction for the sum of the effects after N doses becomes

$$F_s(N,D) = \left[1 - \sum_{i=1}^{N}\frac{D_i}{D_0}\right]^\gamma = \bigotimes_{i=1}^{N} F_s(D_i), \qquad (5)$$

where $\bigotimes_{i=1}^{N}$ denotes the iterated application of the γ-product. On the other hand, if the survival probabilities are independent the effect is not additive and the sum must be redefined as $x \oplus y = x + y - \frac{xy}{\gamma}$. Hence, the total survival fraction is

$$F_s(N,D) = \left[1 - \bigoplus_{i=1}^{N}\frac{D_i}{D_0}\right]^\gamma = \prod_{i=1}^{N} F_s(D_i), \qquad (6)$$

where $\bigoplus_{i=1}^{N}$ denotes the iterated application of the γ-sum.

This equation leads to new insights, as we shall point.

CONSEQUENCES

This model has shown a remarkable agreement with experimental data [7], even in those limits where previous models are less accurate, mainly at high doses. The analysis of the model also provides new hints about the tissue response to radiation: first, the interaction of a tissue with the radiation is universal and characterized by a single exponent (not dependent on the radiation exposure); second, the model includes a cutoff radiation dose above which every single cell dies. Furthermore, previous models can be obtained as particular limiting cases. Besides, as for those models, its mathematical expression is simple and can be easily plotted and interpreted.

Furthermore the model was derived for radiobiological survival fraction but its applicability could be extended to other processes. Indeed, every irreversible phenomena where the individual entities can get a terminal state and that fulfils the conditions: (i) can be described with Tsallis entropy [8], (ii) keeps the maximum entropy principle, (iii) a critical cutoff exists in such a way that no alive entity remains after it, must follow (2).

In particular this could be applied to some biological interactions or clinical treatments as antibiotics or other killer drugs.

Nevertheless the expression (2), understood as survival probability, lacks the extensively property. In other words, for n events following (2) the total survival probability should be found as a composition of the survival probabilities of the successive events. However, there is no straightforward composition rule for those probabilities.

Indeed, a new view introduced by Eq. (6) is that if two doses, X_A and X_B are applied, the resulting probability from their composition has two possible values. If the dose is assumed as additive, $F_{AB} = \left(1 - D_A - D_B\right)^\gamma$ (here D is expressed in units of D_0 to simplify), the individual probabilities under the A and B events could not be treated as independent probabilities, $F_{AB} \neq F_A F_B$. On the other hand, if probabilities are multiplicative, $F_{AB} = \left(1 - D_A\right)^\gamma \left(1 - D_B\right)^\gamma$, doses do not fulfil the superposition principle for the equivalent physical dose, $X_{AB} \neq X_A + X_B$.

In other words, Eq. (6) has revealed, in a formal framework, *the relativity of the applied dose*. This is intuitively known in clinical practice (i.e. doses have not the same effect if continuously applied or splitted in time), but here we have provided a formal basis for this fact, that not only has conceptual importance, but also practical applications, particularly in the isoeffect problem. Results on this issue will be published later.

CONCLUSIONS

A new theoretical expression for the survival fraction of cells under radiation has been found, using the Tsallis formulation of entropy. The existence of a critical value for the absorbed radiation dose under which no entities survive is introduced in the formulation in order to get a proper expression. The new expression depends of two coefficients that characterize the tissue behavior under radiation (γ) and the specific conditions in which the radiation is applied (D_0). Here, the relation between the additivity of the dose and the survival probability has been revealed and conceptualized.

[1] M Tubiana, *Introduction to Radiobiology*, (Taylor & Francis, London, 1990).
[2] C. Tsallis, Braz. J. Phys. **29**, 1 (1999).
[3] E. M. F. Curado and C. Tsallis, J. Phys. A: Math. Gen. **24**, L69 (1991).
[4] C. Tsallis, *Introduction to nonextensive statistical mechanics*, (Springer, New York, 2009).
[5] A. Plastino and A. R. Plastino, Braz. J. Phys. **29**, 50 (1999).
[6] G. G. Steel, in *Basic Clinical Radiobiology for Radiation Oncologists*, edited by G. G. Steel (Edward Arnold Publishers, London, 1993).
[7] O. Sotolongo-Grau, D. Rodríguez-Pérez, J. C. Antoranz and O. Sotolongo-Costa. Phys. Rev. Lett. **105**, 158105 (2010).
[8] O. Sotolongo-Grau, D. Rodríguez-Pérez, J. C. Antoranz and O. Sotolongo-Costa, in *Bayesian inference and maximum entropy methods in science and engineering*, edited by A. Mohammad-Djafari, J. -F. Bercher and P. Bessiere (AIP Conference Proceedings **1305**, 219 (2010)).

MULTICANONICAL DISTRIBUTION AND THE ORIGIN OF POWER LAWS

LA DISTRIBUCIÓN MULTICANÓNICA Y EL ORIGEN DE LAS LEYES DE POTENCIA

G. L. Vasconcelos[a †] and D. S. P. Salazar[b]

a) Departamento de Física, Universidade Federal de Pernambuco, Brazil, giovani@df.ufpe.br†
b) Unidade de Educação a Distância e Tecnologia, Universidade Federal Rural de Pernambuco, Brazil
† corresponding author

A multicanonical formalism is applied to the problem of statistical equilibrium in a complex system with a hierarchy of dynamical structures. At the small scales the system is in quasi-equilibrium and follows a Maxwell-Boltzmann distribution with a slowly fluctuating temperature. The probability distribution for the temperature is determined using Bayesian analysis and it is then used to average the Maxwell-Boltzmann distribution. The resulting energy distribution law is written in terms of generalized hypergeometric functions, which display power-law tails.

Se aplica un formalismo multicanónico al problema del equilibrio estadístico en un sistema complejo con una jerarquía de estructuras dinámicas. A escalas pequeñas el sistema está en cuasi-equilibrio y sigue una distribución de Maxwell-Boltzmann con una temperatura fluctuante. La distribución de probabilidades de la temperatura se determina utilizando el análisis bayesiano y luego esta es usada para promediar la distribución de Maxwell-Boltzmann. La ley de distribución de energía resultante se escribe en términos de funciones hipergeométricas generalizadas, que muestran una cola tipo ley de potencia.

PACS: Complex systems, 89.75.-k; classical ensemble theory, 05.20.Gg; distribution theory, 02.50.Ng

INTRODUCTION

Power law distributions occur in widely diverse physical systems spanning an impressive range of length scales [1]. The appearance of heavy-tailed distributions is often traced to the presence of hierarchical structures in the system [2], whose complex "interaction" may result in violation of the statistical independence of subsystems, thus leading to non-Gibbsian distributions [3]. Despite these insights and the many contributions to the problem [4], it is fair to say that the physical mechanisms behind the emergence of power-law distributions are not yet well understood.

Recently, we introduced [6] a general formalism to describe statistical equilibrium of complex systems with multiple scales where the probability distribution of states displays power-law tails. In this formalism, the hierarchical structure embedding the system of interest is effectively modeled as a set of nested "internal heat reservoirs," where each "reservoir" is described by only one effective degree of freedom, namely, its "temperature." On the basis of a few physically reasonable assumptions, it was possible to show that for a large class of systems the equilibrium distribution can be written explicitly in terms of certain generalized hypergeometric functions, which exhibit power law tails. This family of generalized hypergeometric (GHG) distributions includes, as its first two members, the Boltzmann-Gibbs distribution and the Tsallis distribution [7]. Higher-order members of the GHG family of distributions have been shown to describe remarkably well the statistics of velocity fluctuations in turbulence [5].

The GHG distribution represents a generalization of the canonical distribution for multiscale systems and hence it is also called multicanonical. The main purpose of the present paper is to give an alternative derivation, based on Bayesian analysis, of the multicanonical distribution. Because the derivation of the multicanonical distribution given here tries to parallel (whenever possible) the usual treatment of the canonical distribution, we shall begin our presentation by briefly reviewing the derivation of the canonical distribution.

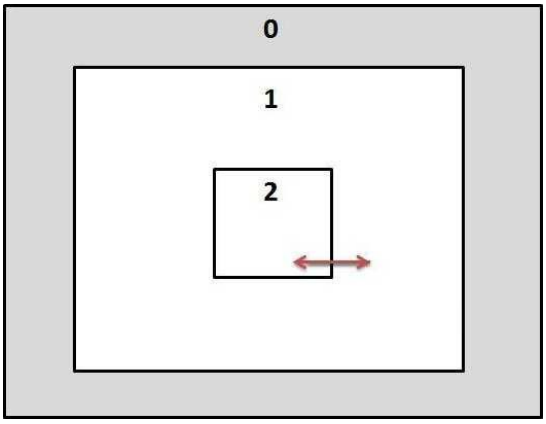

Figure 1: A canonical system in thermal equilibrium at temperature T_0. Arrows indicate energy exchange between the subsystems.

THE CANONICAL DISTRIBUTION

Consider a system in thermal equilibrium at some temperature T_0. We recall that in the canonical formalism the constant temperature constraint is enforced by embedding the system is a much larger system (i.e., a heat bath) capable of giving it energy [8]. We designate the system of interest by the label 2 and the larger system embedding it by the label 1, with the combined system formed by subsystems 1 and 2 being given the label 0; see Fig. 1.

The energies of systems 1 and 2 will be denoted by E_k^1 and E_i^2, respectively, where i and k represent the labels designating the possible states in each system. Let us denote by $p_0(E_{k,i}) = p_0(E_k^1 + E_i^2)$ the probability of finding system 0 in a state corresponding to energy $E_{k,i} = E_k^1 + E_i^2$. In view of the independence between systems 1 and 2, one can then write

$$p_0(E_k + E_i) = p_1(E_k)p_2(E_i), \tag{1}$$

where $p_1(E_k)$ and $p_2(E_i)$ are the probabilities of finding systems 1 and 2 in states with energy E_k and E_i, respectively. Taking the logarithm derivative of (1) with respect to E_k yields

$$\frac{\partial \ln p_0(E_i + E_k)}{\partial E_k} = \frac{d \ln p_1(E_k)}{dE_k} \equiv -\beta_1, \tag{2}$$

where β_1 may be a function of E_k but not of E_i. On the other hand, it is clear that

$$\frac{\partial \ln p_0}{\partial E_k} = \frac{\partial \ln p_0}{\partial E_i} = \frac{d \ln p_2(E_i)}{dE_i}. \tag{3}$$

Comparing (2) and (3), one then concludes that

$$\frac{d \ln p_2(E_i)}{dE_i} = -\beta_1. \tag{4}$$

Since β_1 does not depend on E_i, the preceding equation can be readily integrated, yielding

$$p_2(E_i \mid \beta_1) = constant \cdot \exp(-\beta_1 E_i). \tag{5}$$

Since the partition of system 0 into subsystems 1 and 2 is entirely arbitrary, the quantity β_1 must be the same for any partition one chooses. In other words, β_1 is a characteristic of system 0 only, that is,

$$\beta_1 = \beta_0, \tag{6}$$

which implies that

$$p_2(E_i \mid \beta_0) = A \exp(-\beta_0 E_i), \tag{7}$$

where A is a constant.

It should be evident that the discussion above is completely symmetrical with respect to labels 1 and 2, so that system 2 (irrespective of its size) obeys the same distribution law as system 1. In then follows from (1) and (7) that the probability of finding any subsystem of system 0 in a state with energy E is given by the Boltzmann-Gibbs (BG) distribution:

$$p(E \mid \beta_0) = \frac{g(E)\exp(-\beta_0 E)}{Z_0(\beta_0)}, \tag{8}$$

where $g(E)$ is the density of states and

$$Z_0(\beta) = \int_0^\infty g(E)\exp(-\beta E)dE \tag{9}$$

is the partition function.

It is important to emphasize here that the key step in deriving (8) was the ability to partition the system into two independent subsystems of arbitrary sizes, so that each subsystem is described by the same distribution law. There are however many physical systems, where the relevant probability distributions depend on the scale at which the measurements are made. In such complex systems, the system cannot be partitioned into independent subsystems of arbitrary sizes, and one has to treat each dynamical scale separately, as discussed next.

THE MULTICANONICAL DISTRIBUTION

Here we consider a multiscale system of size L in thermal equilibrium at temperature T_0. We assume that the system possesses a hierarchy of dynamical structures of characteristic sizes $\ell_i = L/b^{i-1}$, with $i = 1, 2, ..., n$, where b is a number greater than 1. (The specific value of b is not relevant here.) We suppose furthermore that there is a wide separation of time scales within this hierarchy with smaller structures having shorter characteristic times. Let us now consider a partition of our system into "nested" subsystems of sizes ℓ_j, as indicated in Fig. 2. We shall designate the subsystem of size ℓ_j by the label j. The "thermodynamic state" of each subsystem j will be characterized by only one parameter, namely, its inverse temperature β_j. As before, we designate the combined system consisting of all subsystems by the label 0.

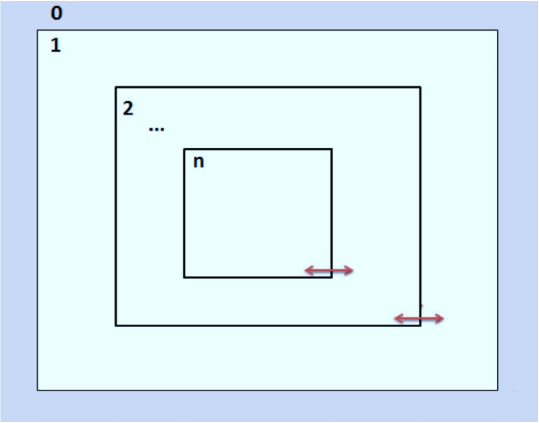

Figure 2: A multicanonical system in thermal equilibrium at temperature T_0.

Let us now focus our attention on the subsystem n of size ℓ_n. Since ℓ_n is the smallest characteristic length scale in the system, it is clear that this subsystem can be arbitrarily divided into two independent subsystems. Thus, repeating the same reasoning that led to Eq. (8), one obtains that the energy distribution law

for this subsystem is given by

$$p(E \mid \beta_n) = \frac{g(E)\exp(-\beta_n E)}{Z_0(\beta_n)}. \quad (10)$$

Note, however, that owing to the (intermittent) energy exchange between subsystem n and its immediate surrounding, represented by subsystem $n-1$, the parameter β_n is no longer constant but rather will fluctuate randomly. If we denote by $f(\beta_n)$ the probability density function (PDF) of β_n, then the marginal distribution $p(E)$ for subsystem n reads

$$p(E) = g(E)\int_0^\infty \frac{\exp(-\beta_n E)}{Z_0(\beta_n)} f(\beta_n)\, d\beta_n. \quad (11)$$

Next we wish to compute $f(\beta_n)$. To do so, we shall make use of Bayesian analysis [9]. First recall that subsystem n is embedded in a much larger subsystem $n-1$, characterized by the parameter β_{n-1}, which is assumed to vary much slower than β_n. We are thus interested in computing $f(\beta_n|\beta_{n-1})$. From Bayes' theorem [9] one has

$$f(\beta_n;\beta_{n-1} \mid E) \propto p(E \mid \beta_n) f(\beta_n;\beta_{n-1}), \quad (12)$$

where β_{n-1} is considered a (hyper)parameter of the distribution of β_n. In Bayesian parlance, the distribution $f(\beta_n;\beta_{n-1})$ is called the prior distribution, $p(E|\beta_n)$ is the likelihood function, and $f(\beta_n;\beta_{n-1}|E)$ is the posterior distribution. [In Eq. (12) we introduced the notation $f(\beta_n;\beta_{n-1}) \equiv f(\beta_n|\beta_{n-1})$ for convenience.]

Let us assume, as is often done in Bayesian analysis, that the prior distribution is conjugate to the likelihood $p(E|\beta_n)$, meaning that the posterior distribution follows the same parametric form as the prior distribution. If we consider the rather general case where $g(E) \propto E^{\gamma-1}$, $\gamma > 0$, so that $Z_0(\beta_n) \propto \beta_n^{-\gamma}$, it then follows from Eq. (8) that $p(E|\beta_n)$ is given by

$$p(E \mid \beta_n) \propto \beta_n^{\gamma} E^{\gamma-1} \exp(-\beta_n E), \quad (13)$$

which when viewed as the likelihood of the parameter β_n is proportional to a gamma distribution. Now, it is well known [9] that in this case the conjugate prior is also a gamma distribution, and so we have

$$f(\beta_n \mid \beta_{n-1}) = \frac{1}{\beta_n \Gamma(\alpha+1)}\left(\frac{\alpha\beta_n}{\beta_{n-1}}\right)^{\alpha+1} \exp\left(-\frac{\alpha\beta_n}{\beta_{n-1}}\right), \quad (14)$$

where α is a constant. In obtaining Eq. (14) we also used the fact that $\langle \beta_n \mid \beta_{n-1} \rangle = \beta_{n-1}$, as it should, since subsystem $n-1$ acts as a heat reservoir for subsystem n. By scale invariance, we assume that the distribution $f(\beta_j|\beta_{j-1})$, for $j = 1, ..., n$, has the same form as in Eq. (14).

We now have

$$f(\beta_n) = \int_0^\infty f(\beta_n \mid \beta_{n-1}) f(\beta_{n-1}) d\beta_{n-1}. \quad (15)$$

Using this relation recursively then yields

$$f(\beta_n) = \int_0^\infty \cdots \int_0^\infty \prod_{j=1}^{n} f(\beta_j \mid \beta_{j-1}) d\beta_1 \cdots d\beta_{n-1}, \quad (16)$$

with $f(\beta_j|\beta_{j-1})$ given by Eq. (14). After inserting Eq. (16) into Eq. (11), and performing a sequence of changes of variables of the type $x_j = \alpha_j \beta_j / \beta_{j-1}$, one can show that the resulting multidimensional integral can be expressed in terms of known higher transcendental functions:

$$p(E) = \frac{g(E)}{Z_n}\, {}_nF_0(\alpha+\gamma+1,\ldots,\alpha+\gamma+1;-\beta_0\alpha^{-n}E), \quad (17)$$

where ${}_nF_0(\alpha_1, ..., \alpha_n; -z)$ is the generalized hypergeometric function of order $(n, 0)$ [10]. The small-scale partition function, Z_n, is given by

$$Z_n = Z_0(\beta_0)\left[\frac{\alpha^{\gamma}\Gamma(\alpha+1)}{\Gamma(\alpha+\gamma+1)}\right]^n. \quad (18)$$

One important property of the generalized hypergeometric (GHG) distribution given in (17) is that it exhibits power-law tails of the form: $p(E) \propto E^{-(\alpha+2)}$, for $E \to \infty$. This follows immediately from the asymptotic expansion of the function ${}_nF_0$ [11]: ${}_nF_0(\alpha_1, ..., \alpha_n; -x) = \Sigma_{i=1}^{n} C_i x^{-\alpha_n}(1+O(1/x))$, as $x \to \infty$. It is also worth pointing out that the first two members of the family ${}_nF_0$ yield elementary functions, namely, ${}_0F_0(x) = \exp(x)$ and ${}_1F_0(1/(q-1), x) = \exp_q(x/(q-1))$, where $\exp_q(x)$ is the q-exponential: $\exp_q(x) = [1 + (1-q)x]^{1/(1-q)}$. The GHG distribution with $n = 0$ thus recovers the Boltzmann-Gibbs distribution, whereas for $n = 1$ it gives the q-exponential or Tsallis distribution [7]. One then sees from the preceding discussion that if a system with only one time scale is in thermal equilibrium then the Boltzmann-Gibbs distribution follows, whereas if it has two distinct time scales the Tsallis distribution should be applicable. For complex systems with more than two characteristic time scales, such as turbulent flows, GHG distributions of higher order are thus required [5, 6].

CONCLUSIONS

We have presented an alternative derivation, based on Bayesian analysis, of the multicanonical distribution, which describes the statistical equilibrium of complex systems possessing a hierarchy of time and length scales. We have shown that the multicanonical distribution can be written explicitly in terms of generalized hypergeometric functions, which exhibit a power-law asymptotic behavior. This thus shows that the emergence of power law distributions —an ubiquitous feature in nature— is intimately connected with the existence of multiple time and length scales in the system.

ACKNOWLEDGEMENTS

This work was supported in part by the Brazilian agencies CNPq and FACEPE

[1] A. Clauset, C. R. Shalizi and M. E. J. Newman, SIAM Review **51**, 661 (2009).
[2] E. Alvarez-Lacalle, B. Dorow, J. -P. Eckmann and E. Moses, Proc. Natl. Acad. Sci. USA **103**, 7956 (2006).
[3] R. A. Treumann and C. H. Jaroschek, Phys. Rev. Lett. **100**, 155005 (2008).
[4] An extensive bibliography on power-law distributions can be found in http://www.nslij-genetics.org/wli/zipf.
[5] D. S. P. Salazar, and G. L. Vasconcelos, Phys. Rev. E **82**, 047301(2010).
[6] D. S. P. Salazar, and G. L. Vasconcelos, submitted to Phys. Rev. Lett. (2012).
[7] C. Tsallis, J. Stat. Phys. **52**, 479 (1988).
[8] G. H. Wannier, *Statistical Physics* (Dover, New York,1966)
[9] A. Gelman, J. B. Carlin, H. S. Stern and D. Rubin, *Bayesian Data Analysis*, 2nd ed. (Chapman and Hall, London, 2003).
[10] A. Erdélyi, W. Magnus, F. Oberhettinger and F. G. Tricomi, *Higher Transcendental Functions,* (McGraw-Hill, New York, 1953).
[11] See, e.g., http://functions.wolfram.com/07.31.06.0041.01

A PENTABLOCK POLYMER FORMING CORE-SHELL STRUCTURES

POLÍMEROS PENTABLOQUES QUE FORMAN ESTRUCTURAS "CORE-SHELL"

K. D. Knudsen[a †], N. Beheshti[b], K. Zhu[b], A. -L. Kjoniksen[b] and B. Nystrom[b]

a) Physics Department, Institute for Energy Technology, N-2027 Kjeller, Norway, kenneth.knudsen@ife.no†
b) Department of Chemistry, University of Oslo, N-0315 Oslo, Norway
† corresponding author

In order to elucidate the interplay between hydrophobic and hydrophilic forces as well as electrostatic interactions for a polymer in an aqueous environment, we recently designed a new pentablock polymer, with the configuration ABCBA. This is a linear chain, where two hydrophobic blocks (B) have been attached to each side of a hydrophilic segment (C), and with negatively charged groups (A) at the ends of the chain. In this system there will be a competition between the attractive forces of the hydrophobic blocks, the repulsion between the charged groups, and the tendency for the hydrophilic group to maximize the interaction with the surrounding water. The polymer was made in two versions, with different lengths of the hydrophilic block, having 34 and 77 segments, respectively. We observed that the physical properties of the system are highly dependent on the length of this C block. A sharp and highly reproducible temperature-induced transition, related to changes in chain conformation, is seen at a temperature around 37 *°C*. The reason for this behavior, as well as the robustness of the transitions discussed.

Con el objetivo de dilucidar la relación entre las fuerzas hidrofóbicas e hidrofílicas, así como de las interacciones electrostáticas para un polímero en ambiente acuoso, hemos diseñado recientemente un nuevo polímero penta-bloque, con la configuración ABCBA. Se trata de una cadena lineal, donde se han unido dos bloques hidrofóbicos (B) a cada costado de un segmento hidrofílico (C), y que posee grupos cargados negativamente (A), en los extremos de la cadena. En este sistema hay una competencia entre las fuerzas atractivas de los bloques hidrofóbicos, la repulsión entre los grupos cargados, y la tendencia del grupo hidrofílico a maximizar la interacción con el agua circundante. El polímero se obtuvo en dos versiones, con diferentes longitudes del bloque hidrofílico de 34 y 77 segmentos, respectivamente. Las propiedades físicas del sistema dependen fuertemente de la longitud del bloque C. Se observa una fuerte transición inducida por temperatura altamente reproducible, alrededor de los 37 °C, relacionada a cambios en la conformación de la cadena. Se discute la causa de este comportamiento, así como la robustez de la mencionada transición.

PACS: Polymer solutions flow properties, 47.57.Ng; structure of polymer solutions , 61.25.he; preparation of polymers, 81.05.g

INTRODUCTION

A fascinating property of so-called amphiphilic block copolymers is their ability to self-assemble into micelles, vesicles, and gels of various morphologies. This can occur as a response to environmental stimuli, e.g. by incorporating temperature-responsive blocks [1]. The term amphiphilic here refers to the different properties represented by two distinct blocks along the same chain, here hydrophilic ("water-friendly") and hydrophobic ("water-unfriendly") blocks. These polymers belong to an important class of materials with a large number of applications, including drug delivery systems, adaptive lubricants, and "smart" surface coatings [2-7]. Most of the previous studies on water-soluble copolymers have been focused on diblock and triblock systems [8-14]. However, we have recently started working with copolymers with up to five well-defined blocks along the chain (pentablock polymer), which opens up for a more complex range of interactions and behaviors in the system.

We here look specifically at results obtained on a ABCBA pentablock copolymer with different lengths of the hydrophilic C-block (cfr. Figure 1). It consists of one hydrophilic *poly(ethylene glycol)block* (PEG, block C), two thermo-sensitive *poly(-Nisopropylacrylamide)blocks* (PNIPAAM, block B), and an anionic *poly(4-styrenesulfonic acidsodium)* (PSSS, block A) block at both ends of the copolymer chain.

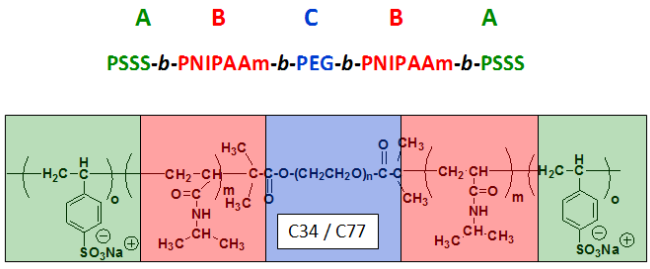

Figure 1: Schematics of the pentablock polymer used in this work. The color codes refer to hydrophobic (red), hydrophilic (blue), and charged groups (green). Here the repetition numbers for the A/B blocks are 12/63 (C34) and 14/65 (C77), respectively.

PNIPAAM is employed here since it is a highly sensitive thermoresponsive polymer that is able to associate and

contract above its so-called lower critical solution temperature (LCST) of ca. 32 ^oC, when being alone in solution [15]. The charged block at both ends of the chain are here introduced as an extra element of control in the system. It will amongst other factors ensure a high degree of solubility of the copolymer in water. Since the B-block becomes hydrophobic at a certain temperature, one may expect this block to combine with similar blocks from other chains and expel water, thus forming a nano-sized micellar structure.

It is of interest here to look at what kind of forces are expected to be present in this system. For polymer chains dissolved in water, there is usually a fine balance between several forces -all around or slightly higher than k_BT- that determine the actual conformation of the chain. In the case of the polymer chain studied here, we expect there to be a contribution from hydrophobic forces (entropy change for water), hydrophilic (e.g. hydrogen bonds with water molecules), Coulombic (due to the charged end groups), as well as the contribution to entropy (positive ΔS) upon any liberation of counterions from the polymer. Thus a conformational change as that depicted schematically in Figure 2 may be induced by one of these contributions dominating slightly over the others for an individual segment (monomer), and being strongly amplified by the fact that the polymer chain contains a large number of segments.

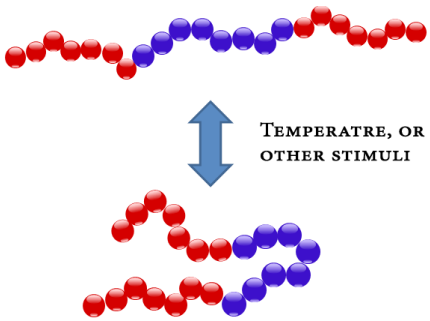

Figure 2. Simple schematics of conformational change for a polymer chain with hydrophobic (red) and hydrophilic (blue) segments.

This paper presents a summary of recent results obtained with this system, and will empasize how the length of the PEG block has a large impact on the temperature- induced viscosity and structure of the polymer. We also discuss the reversibility and cyclability of this behavior. More background information on this system can be found in ref. [16].

RESULTS AND DISCUSSION

In order to elucidate the association behavior in polymer systems, measurement of turbidity can be very useful as an initial step. Figure 3 shows how an extremely abrupt transition is observed for this system at a temperature around 37 ^oC upon heating, for both chain lengths studied. The rise of the turbidity with increasing temperature indicates the formation of condensed structures, sufficiently large to scatter light. When the hydrophobic blocks of several chains interact and assemble, these will at elevated temperature contract strongly in order to avoid water exposure if there is a sufficient number of hydrophobic segments present.

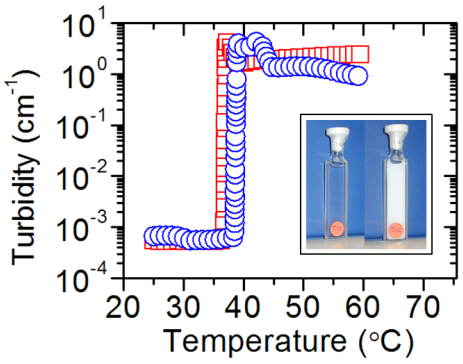

Figure 3. Change of turbidity vs. temperature for the C34 (red squares) and C77 (blue circles) system (4 *wt.*%). Inset: visual appearance at 25 ^oC and 50 ^oC for C34.

Also visual inspection of the system reveals that upon heating it becomes highly turbid (see inset Figure 3). Note that these changes were found to be fully reversible, thus the original character is regained upon cooling below the threshold. A series of new measurements, obtained after those presented in ref. [16] and during an extended period of several months, have shown that the heating/cooling process can be repeated nearly indefinitely without any observable loss in material properties. This behavior is actually not so common in soft-matter systems, where loss of reversibility and aggregation/ageing is seen very often. We believe that the main reason for this important property for the present system is the use of heavily charged end blocks, which stabilize the system and introduce a marked robustness in its behavior.

To gain further insight into this system, shear viscosity measurements were performed. A shear flow tends to bring polymer chains close to each other faster than from Brownian motion, thereby speeding up the assembly. This phenomenon is known as "orthokinetic" aggregation and it frequently appears in solutions or suspensions of sticky moieties at low shear rate. At high shear rate, on the other hand, the large association complexes are foreseen to break up under the influence of high shear stresses. The effects of temperature and shear rate on the viscosity of the system are illustrated in Figure 4. A much stronger temperature dependence of the viscosity is found for C77 than for C34, and an incipient shear rate effect is observed at high temperatures for C77, whereas no effect can be discerned for C34. This result clearly shows that interconnected and thus effectively larger species are formed in solutions of C77 at elevated temperatures, while only non-connected assemblies are formed in the C34 system. This interconnection between assemblies is provided by the long C-block. We may note here the dramatic viscosity increase (more than a factor 100) for the system with the longest central block upon a change in temperature. Also this change has now been found to be reproducible after long periods of repeated use.

We furthermore performed small-angle neutron scattering

(SANS) measurements on this system to gain insight about structural changes at the nanoscale. For both C34 and C77 we observe a dramatic change in the SANS pattern with increasing temperature. The low-q scattering increases more than a factor of ten, demonstrating that a significant structural reorganization takes place in the size regime probed by SANS. At 30 ^oC, i.e. below the threshold temperature, there is only weak scattering, as expected for a polymer that exists mainly as individual unfolded chains (unimers). We may here make use of the so-called Debye model [17] i.e. the form factor (P), developed for a flexible linear polymer chain in solution, where the scattering function is given by

$$P(x) = 2[e^{-x} + x - 1]/x^2, \qquad \text{with } x = (qR_G)^2.$$

Here q is the scalar of scattering vector, $q = (4\pi/\lambda)\sin\theta$, where λ is the neutron wavelength and θ is the scattering angle.

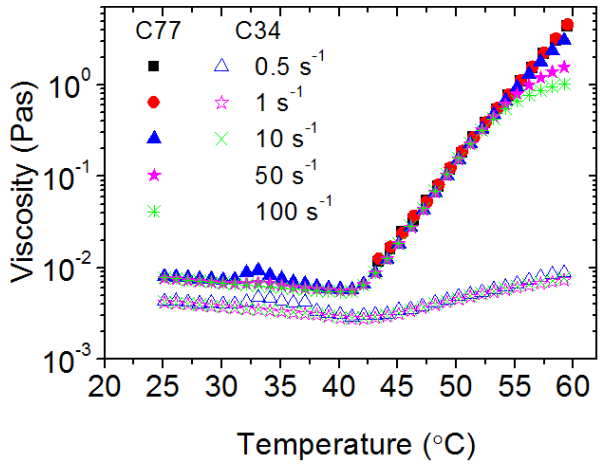

Figure 4. Viscosity dependence on temperature and shear rate, as well as on the length of the hydrophilic block for the two variants of the polymer chain.

This model results in a value for the radius of gyration (RG) of the unimer equal to 29 *Å*, or ca. 3 *nm* (the scattering from C34 and C77 at 30 ^oC cannot be distinguished in this respect). For the high temperature dataset the shape of the SANS data, including the suppression of the scattering at low q-values, encourages the use of a core-shell model [18] to fit the data. Due to the presence of charges it is necessary to include a Coulomb interaction in the model.

When using the core–shell form factor together with a screened Coulomb interaction potential [19] we obtain a good fit for the C77 polymer (as seen in Figure 5), giving an average core radius of 89 *Å* , and a shell thickness of 37 *Å* . This would correspond to an overall particle diameter of 252 *Å* , or ca. 25 *nm*. In this calculation we have employed the already known values of the D_2O scattering length density and the dielectric constant, i.e. 6.3×10^{-6} $Å^{-2}$ and 78, respectively. For the short PEG-chain polymer (C34) the model fit shown in Figure 5 deviates from the data at the lowest q-values, most likely due to the existence of a population of larger particles whose size cannot be determined within this q-range.

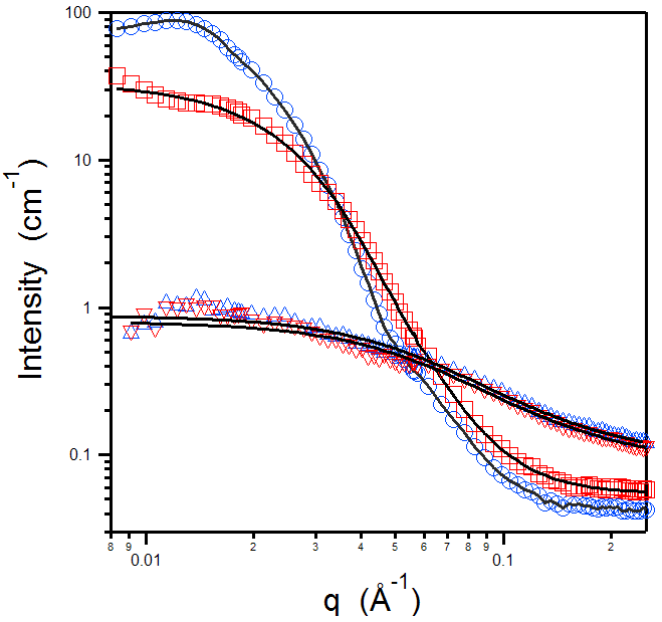

Figure 5. SANS patterns for C34 (red squares) and C77 (blue circles) at 50 ^oC and at 30 ^oC (triangles).

Overall, the SANS study shows clearly how these chains assemble to form core-shell particles upon a temperature increase above the transition, which was found to be at ca. 37 ^oC.

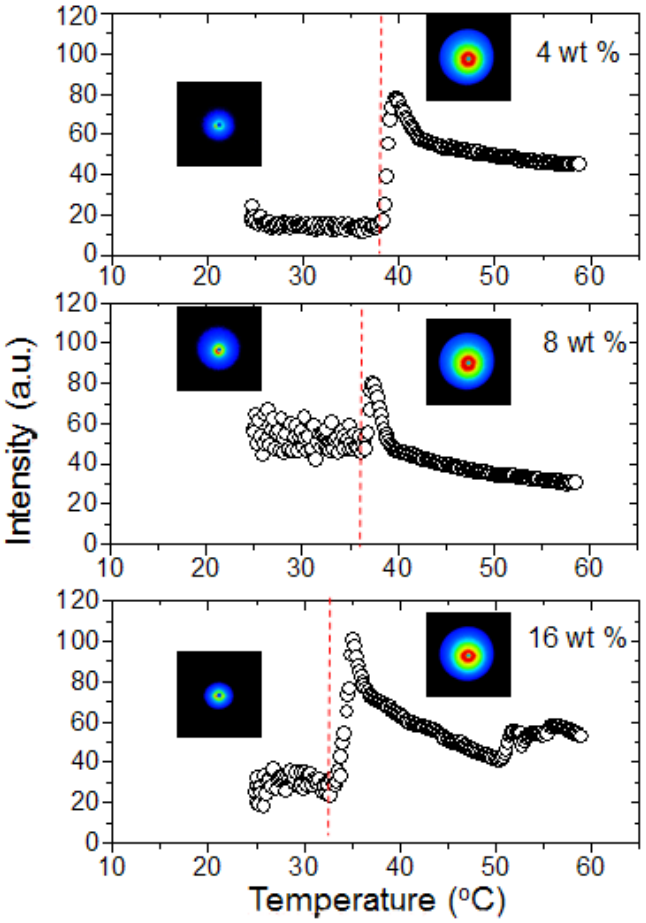

Figure 6: Small angle light-scattering (SALS) intensity vs. temperature for three different concentrations of the C34 system; 4, 8, and 16 *wt.%*. The insets show the 2D SALS patterns at low temperature and at the peak of the transition.

We have recently also studied the effect of polymer concentration on the behavior of this system. It is found that the transition temperature can be moved down in steps upon an increase in concentration. This is illustrated in Figure 6, where the change in light scattering intensity was used to probe the system through the transition region.

It can here be seen how the initial transition temperature just above 37 ^oC (4 *wt.*%) is shifted towards 35 ^oC and subsequently to 32 ^oC for the 8 and 16 *wt.*% systems, respectively. However, the increased concentration will also have strong influence on the polymer chain conformation and interaction between chains, effects that need further studies to be clarified in detail.

CONCLUSIONS

We have revisited our recent studies on thermoresponsive polymers, with a particular focus on a pentablock system (ABCBA). It is shown how a highly abrupt transition from extended chains to globular entities can be induced by proper combination of hydrophilic and hydrophobic elements. Repeated studies have shown that this behavior is not only fully reversible, but shows no signs of ageing even over extended periods of time. We have reason to believe that the incorporation of charged end groups is an important element in this respect. The well-defined changes observed in opacity together with the cyclability could be of interest in connection with e.g. adaptable surface layers without the need for external (e.g. electrical) connections.

ACKNOWLEDGMENTS

K. Z. and B. N. acknowledge support from the Norwegian Research Council through the project 177665/V30.

[1] *Block Copolymers in Nanoscience*, Ed. M. Lazzari, G. Liu, S. Lecommandoux, (Wiley-VCH, Weinheim, 2006).
[2] V. Sfika and C. Tsitsilianis, Macromolecules **37**, 9551 (2004).
[3] X. Y. Xiong, K. C. Tam and L. H. Gan, Polymer **46**, 1841 (2005).
[4] C. Xu, X. Fu, M. Fryd, S. Xu, B. B. Wayland, K. I. Winey andR. J. Composto, Nano Lett. **6**, 282 (2006).
[5] J. F. Tan, P. Ravi, H. P. Too, T. A. Hatton and K. C. Tam, Biomacromolecules **6**, 498 (2005).
[6] Y. Liu, V. Klep, B. Zdyrko and I. Luzinov, Langmuir **21**, 11806 (2005).
[7] Y. Kim, J. Pyun, J. M. J. Frechet, C. J. Hawker and C. Frank, Langmuir **21**, 10444 (2005).
[8] B. Svensson, U. Olsson and P. Alexandridis, Langmuir **16**, 6839 (2000).
[9] X. Zhao, W. Liu, D. Chen, X. Lin and W. W. Lu, Macromol. Chem.Phys. **208**, 1773 (2007).
[10] K. Zhu, R. Pamies, A.-L. Kjøniksen and B. Nystrom, Langmuir **24**, 14227 (2008).
[11] A. -L. Kjøniksen, K. Zhu, R. Pamies and B. Nystrom, J. Phys. Chem. B **112**, 3294 (2008).
[12] T. Ueki, M. Watanabe and T. Lodge, Macromolecules **42**, 1315 (2009).
[13] S. Reinicke, J. Schmelz, A. Lapp, M. Karg, T. Hellweg and H. Schmalz, Soft Matter **5**, 2648 (2009).
[14] S. De Santis, R. D. Ladogana, M. Diociaiuti and G. Masci, Macromolecules **43**, 1992 (2010).
[15] H. G. Schild, Prog. Polym. Sci. **17**, 163 (1992).
[16] N. Beheshti, K. Zhu, A. -L. Kjøniksen, K. D. Knudsen, B. Nyström, Soft Matter **7**, 1168 (2011).
[17] R. -J. Roe, *Methods of X-Ray and Neutron Scattering in Polymer Science*, (Oxford University Press, New York, 2000).
[18] J. B. Hayter, in *Physics of Amphiphiles–Micelles, Vesicles, and Microemulsions.* Ed. V. de Giorgio and M. Corti, (North Holland, Amsterdam, pp. 59–93, 1983).
[19] J. B. Hayter and J. Penfold, Mol. Phys. **42**, 109 (1981).

THE FREDERIKS TRANSITION IN AN AQUEOUS CLAY DISPERSION

LA TRANSICIÓN DE FREDERIKS EN UNA DISPERSIÓN ACUOSA DE ARCILLA

H. Hemmen, E. L. Hansen, N. I. Ringdal and J. O. Fossum†

Department of Physics, NTNU, Trondheim, Norway, jon.fossum@ntnu.no†
† corresponding author

We show that under certain circumstances, aqueous dispersions of Na-fluorohectorite synthetic clay display transient spatially periodic structures when subjected to magnetic fields. These nematic structures result from the deformation of a uniform director pattern, a phenomenon which is known as the Frederiks transition. We study the samples between crossed polarizers, and present birefringence images of the particle reorganization as a function of time. Repeated measurements at different magnetic field strengths show that the threshold value for the inhomogeneous Frederiks transition with this setup is just below 0.5 *T*, and that the spatial wavelength of the structures decreases when the magnetic field is increased, as is expected.

Se muestra que, bajo ciertas circunstancias, las dispersiones acuosas de arcilla sintética de Na-fluorohectorita exhiben estructuras espacialmente periódicas transitorias, cuando se someten a campos magnéticos. Tales estructuras nemáticas resultan de la deformación de un patrón uniforme director, un fenómeno que se conoce como la transición de Frederiks. Se estudian las muestras entre polarizadores cruzados, y las imágenes de birrefringencia de la reorganización de partículas en función del tiempo. Las mediciones repetidas con diferente intensidad de campo magnético, muestran que el valor umbral de la transición de Frederiks inhomogénea con esta configuración está justo por debajo de 0.5 *T*, y que la longitud de onda espacial de las estructuras disminuye cuando el campo magnético se incrementa, como es de esperar.

PACS: Structure of nematic liquid crystals, 61.30.-v; phase separation and segregation in colloids, 64.75.Xc; birefringence in bulk materials and thin films, 78.20.Fm

The Frederiks transition [1] is a phenomenon occurring in liquid crystals when a field is used to realign the nematic director away from its (field-free) equilibrium position. The path between the initial and final states often involve transient, spatially periodic structures, where adjacent domains rotate in opposite directions [2-3]. Due to its usefulness for determining material properties of liquid crystals (e.g. the elastic constant of the mode involved in the distortion), several theoretical and experimental studies have been performed on the Frederiks transition, both with rod-like and disk-like molecules (see e.g. [4-6]).

Liquid crystalline order in aqueous clay dispersions has attracted attention in recent years, see e.g. [7-10]. Here we report an observation of the Frederiks transition in dispersions containing the synthetic smectite clay Na-fluorohectorite. When mixed in water and left to phase separate over time, this system develops several coexisting phases in a single sample tube [7]. From bottom to top, these are: an isotropic gel region, a nematic gel region, a nematic sol region, and an isotropic sol. Due to the comparatively high viscosity and shear thinning behavior of the nematic gel, its dynamic response to magnetic fields is strongly damped [11]. However, the liquid-like nematic sol has been shown to respond relatively fast to magnetic fields [7], allowing particle reorientation with fields on the order of 0.1 *T*.

The samples used for the present experiments were dispersions of 3 % *w*/*w* of Na-fluorohectorite in 10^{-3} *M* NaCl suspensions, contained in 2 *mm* diameter glass capillaries. We let the samples settle for 4-5 months, during which the largest particle aggregates sediment out, and the four different regions appear in the samples. Before applying any magnetic fields, the clay particles in the nematic sol orient antinematically, i.e. with their particle normals spread out in the plane perpendicular to the capillary axis [7]. This is due to the circular geometry of the capillary, and the fact that the disk-like particles anchor homeotropically to interfaces [7].

In order to induce the Frederiks transition, a magnetic field of about 1 Tesla was first applied to the nematic sol phase perpendicular to the capillary axis. Due to the negative diamagnetic susceptibility anisotropy of the particles, they respond to magnetic fields by orienting their plate normals perpendicular to the magnetic field lines. Combined with the influence of the particles that are homeotropically anchored to the capillary walls, the field acts to change the nematic configuration from antinematic to uniaxial nematic, with the particle normals oriented on average along a common direction in the horizontal plane, perpendicular to the magnetic field lines.

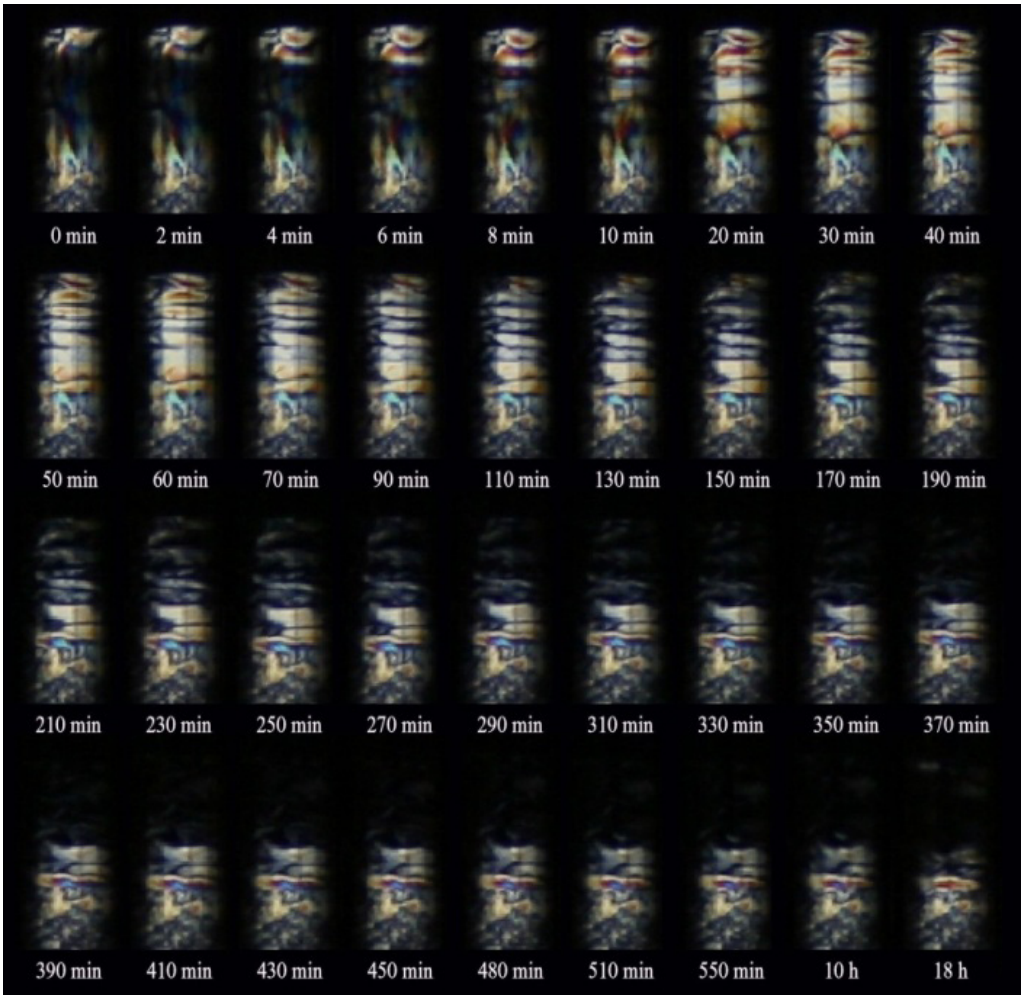

Figure 1: Photo series of the reorientation process of a nematic phase in a 1 T magnetic field. The particles are initially aligned with the director horizontally in the paper plane, and a reorientation is triggered by applying the magnetic field in the same direction. The first sign of stripes appears after a couple of minutes, being most visible in the upper part. After about 8 hours, the majority of the particles are reoriented to a stable configuration where their plate normals point along the line of sight (out of the paper) or vertically, and therefore do not contribute to the birefringence. The vertical black stripes in the pictures are reflections from the magnet

Once this particle configuration was obtained, the capillary was rotated 90 degrees around its axis, thus initially causing the clay plate normals to be aligned in the magnetic field direction. This unstable configuration promoted realignment of the nematic phase. During the subsequent realignment process, visual images were recorded through crossed polarizers, allowing a visualization of the anisotropy in the particle alignment. The polarizers were oriented such that their fast axes were respectively vertical (parallel to the capillary axis), and horizontal (parallel to the magnetic field). A time series of the recorded images with a magnetic field strength of 1 T can be seen in Figure 1. As the magnetic field reorients the particles, transient periodic stripes gradually appear and disappear during the hours-long process of reorientation. The stripes correspond to regions where the particles are oriented with the average plate normal at an angle to the transmission axes of the polarizers.

In systems of platelets with negative diamagnetic susceptibility anisotropy, the non-uniform Frederiks transition is different from that observed in systems with positive diamagnetic susceptibility, in that the first case possesses degeneracy in tilt-angles directions perpendicular to the director axis. For a round flat particle with negative anisotropy of the magnetic susceptibility, a static magnetic field cannot by itself determine which orientation the final director will obtain. In other experiments on systems of disks with this behavior [5-6], the degeneracy is removed by rotating the magnetic field or the sample in the plane normal to the final director orientation.

As these are preliminary measurements, we have not yet modified our setup in this way, and thus we are not yet able to fully characterize the nature of the transition, partly because from birefringence images using only linear polarizers one cannot unambiguously determine the orientation of the particle normals. This could have been achieved using a more complex polarizer setup, e.g. Mueller matrix ellipsometry [12]. However, based on previous experiments using small angle x-ray scattering to determine particle orientation, we expect that the particles in the top part of the nematic sol region reorients to a mainly horizontal alignment (particle normal parallel to the capillary axis), due to the anchoring to the isotropic-nematic interface. After several rotations, all particles will eventually reach this orientation, as it is the only